

Enhanced Long-Lived Dark Photon Signals at the LHC

Mingxuan Du,¹ Zuowei Liu,^{1,2,3,*} and Van Que Tran¹

¹*Department of Physics, Nanjing University, Nanjing 210093, China*

²*Center for High Energy Physics, Peking University, Beijing 100871, China*

³*CAS Center for Excellence in Particle Physics, Beijing 100049, China*

We construct a model in which the standard model is extended by a hidden sector with two gauge $U(1)$ bosons. A Dirac fermion ψ charged under both $U(1)$ fields is introduced in the hidden sector which can be a subcomponent of the dark matter in the Universe. Stueckelberg mass terms between the two new gauge $U(1)$ fields and the hypercharge gauge boson mediate the interactions between the standard model sector and the hidden sector. A remarkable collider signature of this model is the enhanced long-lived dark photon events at the LHC than the conventional dark photon models; the long-lived dark photons in the model can be discriminated from the background by measuring the time delay signal in the precision timing detectors which are proposed to be installed in the LHC upgrades and have an $\mathcal{O}(10)$ pico-second detection efficiency. Searches with current LHCb data are also investigated. Various experimental constraints on the model including collider constraints and cosmological constraints are also discussed.

INTRODUCTION

Recently, particles with a long lifetime have been studied extensively at colliders (see e.g. Ref. [1] for a review). At the large hadron collider (LHC), the long-lived particles have been searched for in channels with displaced dilepton vertices [2–6] and in channels with displaced jets vertices [7–15]. Searches for displaced vertices of collimated leptons or light hadrons with low p_T , which originate from light neutral particles such as dark photons, have been carried out at the LHC, e.g. by the ATLAS collaboration [16, 17].

Typically, for a particle to be considered as a long-lived particle at the LHC, the decay length has to be larger than $\mathcal{O}(1)$ mm so that the displaced vertex can be detected by the spatial resolution of the LHC detectors. Thus, the coupling strength between long-lived particles and the standard model (SM) particles is usually significantly reduced. For example, an electrophilic vector boson A' that couples with electron via $gA'_\mu \bar{e}\gamma^\mu e$ has a decay width $\Gamma = g^2 m_{A'}/(12\pi)$ and a decay length $d = \gamma v\tau$, where v (τ) is the velocity (lifetime) of the vector boson A' , and γ is the Lorentz boost factor. For such a particle to have a macroscopic decay length so that it can give rise to a long-lived particle signature at the LHC, the decay coupling is typically small. For example, consider a typical decay length as $d \simeq 1$ m, one has $g \sim \mathcal{O}(10^{-6})$ for the case where $m_{A'} = 1$ GeV and $\gamma = 100$. Thus simple long-lived vector boson models usually lead to a suppressed LHC cross section due to the small coupling constant needed for the large decay length.

In this paper, we construct a model that predicts a long-lived dark photon (LLDP) with a GeV scale mass. Unlike many other dark photon models, the production cross section of the GeV LLDP in our model at the LHC is not suppressed. This is because the production process of the LLDP is different from its decay process. We use the Stueckelberg mechanism to mediate the interaction

between the hidden sector and the SM sector; the production and decay processes of the LLDPs are mediated by different Stueckelberg mass terms.

Recently, models in which LLDPs can have a sizable collider signal have been proposed in the literature. For example, Ref. [18] introduced a second boson with couplings to both SM quarks and the hidden fermion to produce dark photons at colliders. Ref. [19] used a dimension-five operator between a scalar $SU(2)_L$ triplet, the SM $SU(2)_L$ gauge bosons and the dark gauge boson to generate a non-abelian kinetic mixing term, which can enhance the LLDP signal. Potential large LLDP collider signals can also arise via top-partner decays [20], or via a Higgs portal interaction to the hidden QED [21].

THE MODEL

We introduce two Abelian gauge groups in the hidden sector: $U(1)_F$ with gauge boson X^μ and $U(1)_W$ with gauge boson C^μ . We use the Stueckelberg mechanism to provide masses to the two new gauge bosons in the hidden sector, and also to mediate the interactions between the hidden sector and the SM sector [23–27]. The Lagrangian for the extension is given by $\mathcal{L} = \mathcal{L}_F + \mathcal{L}_W$ where

$$\begin{aligned} -4\mathcal{L}_F &= X_{\mu\nu}^2 + 2(\partial_\mu\sigma_1 + m_1\epsilon_1 B_\mu + m_1 X_\mu)^2, \\ -4\mathcal{L}_W &= C_{\mu\nu}^2 + 2(\partial_\mu\sigma_2 + m_2\epsilon_2 B_\mu + m_2 C_\mu)^2. \end{aligned}$$

Here B_μ is the hypercharge boson in the SM, σ_1 and σ_2 are the axion fields in the Stueckelberg mechanism, and m_1 , m_2 , $m_1\epsilon_1$, and $m_2\epsilon_2$ are mass terms in the Stueckelberg mechanism. The dimensionless parameters ϵ_1 and ϵ_2 are assumed to be small in our analysis: $\epsilon_1 \sim \mathcal{O}(10^{-7})$ and $\epsilon_2 \sim \mathcal{O}(10^{-2})$ for our current analysis at the LHC. \mathcal{L}_F is invariant under $U(1)_Y$ gauge transformations $\delta_Y B_\mu = \partial_\mu \lambda_B$ and $\delta_Y \sigma_1 = -m_1 \epsilon_1 \lambda_B$; \mathcal{L}_F is also invariant under $U(1)_F$ gauge transformation

$\delta_F X_\mu = \partial_\mu \lambda_X$, and $\delta_F \sigma_1 = -m_1 \lambda_X$. Similarly, \mathcal{L}_W is gauge invariant under both $U(1)_Y$ and $U(1)_W$.

In the hidden sector, we further introduce one Dirac fermion ψ that is charged under both $U(1)_F$ and $U(1)_W$. Vector current interactions between the Dirac fermion and the gauge bosons in the hidden sector are assumed, i.e., $g_F \bar{\psi} \gamma^\mu \psi X_\mu + g_W \bar{\psi} \gamma^\mu \psi C_\mu$ where g_F and g_W are the gauge couplings for $U(1)_F$ and $U(1)_W$ respectively.

The two by two mass matrix in the neutral gauge boson sector in the SM is now extended to a four by four mass matrix, which, in the gauge basis $V = (C, X, B, A^3)$, is given by

$$M^2 = \begin{pmatrix} m_2^2 & 0 & m_2^2 \epsilon_2 & 0 \\ 0 & m_1^2 & m_1^2 \epsilon_1 & 0 \\ m_2^2 \epsilon_2 & m_1^2 \epsilon_1 & \sum_{i=1}^2 m_i^2 \epsilon_i^2 + \frac{g'^2 v^2}{4} & -\frac{g' g v^2}{4} \\ 0 & 0 & -\frac{g' g v^2}{4} & \frac{g^2 v^2}{4} \end{pmatrix} \quad (1)$$

where g and g' are gauge couplings for the SM $SU(2)_L$ and $U(1)_Y$ gauge groups respectively, A^3 is the third component of the $SU(2)_L$ gauge bosons, and v is the Higgs vacuum expectation value. The determinant of the mass square matrix vanishes which ensures the existence of a massless mode to be identified as the SM photon.

The mass matrix can be diagonalized via an orthogonal transformation \mathcal{O} such that $\mathcal{O}^T M^2 \mathcal{O} = \text{diag}(m_{Z'}^2, m_{A'}^2, m_Z^2, 0)$; the mass basis $E = (Z', A', Z, A)$ is related to the gauge basis V via $E_i = \mathcal{O}_{ji} V_j$. In the mass basis, A is the SM photon, Z is the SM Z boson, A' is the dark photon with a GeV-scale mass and Z' is the heavy boson with a TeV-scale mass. Diagonalization of the mass matrix leads to interactions between Z/A in the SM to the fermion ψ in the hidden sector, and also interactions between Z'/A' in the hidden sector and SM fermions f ; both $\psi - Z/A$ and $f - Z'/A'$ couplings are suppressed by the small ϵ_1 and ϵ_2 parameters, and vanish in the $\epsilon_1 = 0 = \epsilon_2$ limit.

We parameterize the interactions between the fermions and the mass eigenstates of the neutral bosons via

$$\bar{f} \gamma_\mu (v_i^f - \gamma_5 a_i^f) f E_i^\mu + v_i^\psi \bar{\psi} \gamma_\mu \psi E_i^\mu \quad (2)$$

where the vector and axial-vector couplings are given by

$$v_i^f = (g \mathcal{O}_{4i} - g' \mathcal{O}_{3i}) T_f^3 / 2 + g' \mathcal{O}_{3i} Q_f, \quad (3)$$

$$a_i^f = (g \mathcal{O}_{4i} - g' \mathcal{O}_{3i}) T_f^3 / 2, \quad (4)$$

$$v_i^\psi = g_W \mathcal{O}_{1i} + g_F \mathcal{O}_{2i}, \quad (5)$$

with Q_f is the electric charge of fermion f , T_f^3 is the quantum number of the left-hand chiral component of the fermion f under $SU(2)_L$.

EXPERIMENTAL CONSTRAINTS

Here we discuss various constraints on the model, including electroweak constraints from LEP, constraints

from LHC, and also cosmological constraints.

In our analysis, we will fix most model parameters so that a sizable LHC signal is expected. We first discuss these default parameter values. The heavy Z' boson in our model mostly originates from the $U(1)_W$ boson C_μ whose mass is fixed to be $m_2 = 700$ GeV in the remaining of the analysis. In order to obtain a sufficient large $\psi\bar{\psi}$ production cross section at the LHC, we choose $g_W = 1$; a relatively large $U(1)_F$ coupling constant is also chosen, $g_F = 1.5$, so that a rather sizable dark radiation rate for the ψ particle can be achieved in the model. We use $c\tau = \hbar c / \Gamma = 1$ m as the characteristic value for the proper lifetime of the dark photon, where Γ is the dark photon decay width; the dark photon decay widths are given in Appendix. We find that small modifications around $c\tau = 1$ m do not lead to significant changes in the collider signatures. The above values are the default ones used throughout the analysis, if not explicitly specified.

Z invisible decay: The Z invisible decay width is measured to be $\Gamma_{\text{inv}}^Z \pm \delta\Gamma_{\text{inv}}^Z = 499 \text{ MeV} \pm 1.5 \text{ MeV}$ [28]. The Z boson can decay into the $\psi\bar{\psi}$ final state, if $m_Z > 2m_\psi$, with a decay width

$$\Gamma_{Z \rightarrow \psi\bar{\psi}} = \frac{m_Z}{12\pi} (v_3^\psi)^2 \sqrt{1 - 4x_{\psi Z}} (1 + 2x_{\psi Z}), \quad (6)$$

where $x_{\psi Z} \equiv (m_\psi / m_Z)^2$, and v_3^ψ is the vector coupling between the Z boson and ψ , as given in Eq. (5). Equating the invisible decay width due to the $\psi\bar{\psi}$ final state to the experimental uncertainty $\delta\Gamma_{\text{inv}}^Z$, one obtains an upper bound on v_3^ψ , which is shown on Fig. (1). For light ψ mass, one has $v_3^\psi \gtrsim 2.5 \times 10^{-2}$.

Electroweak constraint on the Z mass: The mass of the Z boson is modified due to the enlarged neutral gauge boson mass matrix, as given in Eq. (1). For the parameter space of interest in our analysis, i.e., $\epsilon_1 \ll \epsilon_2$, the mass shift on the Z boson can be estimated as

$$\left| \frac{\Delta m_Z}{m_Z} \right| \simeq \frac{\epsilon_2^2}{2} s_W^2 \left(1 - \frac{m_Z^2}{m_2^2} \right)^{-1}, \quad (7)$$

where $s_W^2 \equiv \sin^2 \theta_W = 0.22343$ [29], with θ_W being the weak rotation angle. We adopt the methodology in Ref. [24] to estimate the electroweak constraints. The experimental uncertainty of the Z mass is given by [24]

$$\left[\frac{\delta m_Z}{m_Z} \right]^2 = \left[\frac{c_W^{-2} - 2t_W^2}{\delta m_W^{-1} m_W} \right]^2 + \frac{t_W^4 (\delta \Delta r)^2}{4(1 - \Delta r)^2}, \quad (8)$$

where $c_W \equiv \cos \theta_W$, and $t_W \equiv \tan \theta_W$. Here we take into account the recent analysis on the uncertainty of the W boson mass, $m_W \pm \delta m_W = 80.387 \pm 0.016$ GeV [29], and on the radiative correction, $\Delta r \pm \delta \Delta r = 0.03672 \mp 0.00017 \pm 0.00008$ [29] where the first uncertainty is due to the top quark mass and the second is due to the fine structure constant $\alpha(m_Z)$ at the m_Z scale. Adding in quadrature, we obtain $\delta \Delta r = 0.00019$. Equating the mass shift on the Z boson given in Eq. (7) to the

experimental uncertainty, one obtains an upper bound on ϵ_2

$$|\epsilon_2| \lesssim 0.036 \sqrt{1 - (m_Z/m_2)^2}. \quad (9)$$

Di-lepton constraint on Z' decays: Dilepton final states which are produced at the LHC from the heavy Z' boson via the Drell-Yan process, can be searched for by reconstructing their invariant mass. Fig. (1) shows the 95 % CL upper bound on ϵ_2 in the dilepton channel from ATLAS [30].

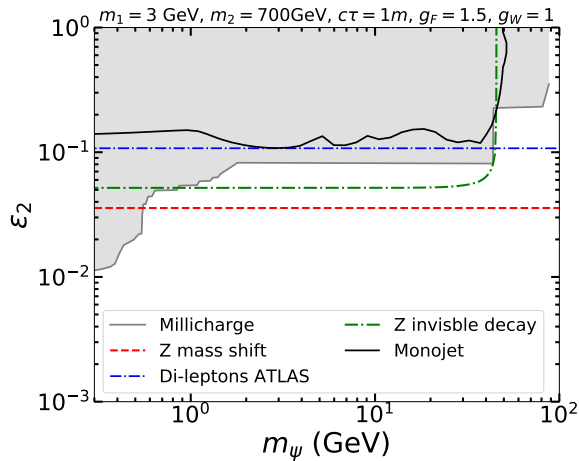


Figure 1. The 95% CL exclusion limits on ϵ_2 as a function of m_ψ . We use the following parameters: $m_1 = 3$ GeV, $m_2 = 700$ GeV, $g_F = 1.5$, $g_W = 1.0$, and $c\tau = 1$ m. Shown are the millicharged particle searches at the colliders (shaded light gray) [31], electroweak constraints due to the Z mass shift (dashed red), the Z invisible decay (dash-dotted green) [28], the di-lepton high mass resonance search at ATLAS (dash-dotted blue) [30], and the mono jet search at ATLAS (solid black) [32].

Constraints on millicharge: Due to the off-diagonal elements in the four by four mass matrix, the ψ particle interacts weakly with the Z boson and the photon in the SM. Thus there is a small electric charge of the ψ particle, $\delta = v_4^\psi/e$, with respect to the photon. In the parameter space of interest of the model, we have $\delta \simeq 0.88 \epsilon_2/e$. The small electric charge is often referred to as ‘‘millicharge’’; the ψ particle remains undetectable in typical particle detectors due to the minute electric charge. Fig. (1) shows the collider constraints on millicharge in the (m_ψ, ϵ_2) plane [31]. The collider constraints on millicharge are the most stringent constraints on ϵ_2 for $m_\psi \lesssim 0.6$ GeV.

Because the ψ particle is charged under $U(1)_W$ and $U(1)_F$ in the hidden sector, it is stable and thus can be a dark matter (DM) candidate. For the parameter space of interest, i.e., $m_\psi > m_{A'}$, the annihilation channel into on-shell dark photons, $\psi\bar{\psi} \rightarrow A'A'$, is the dominant process for the relic abundance of the ψ particle; the annihilation cross section can be approximated as follows

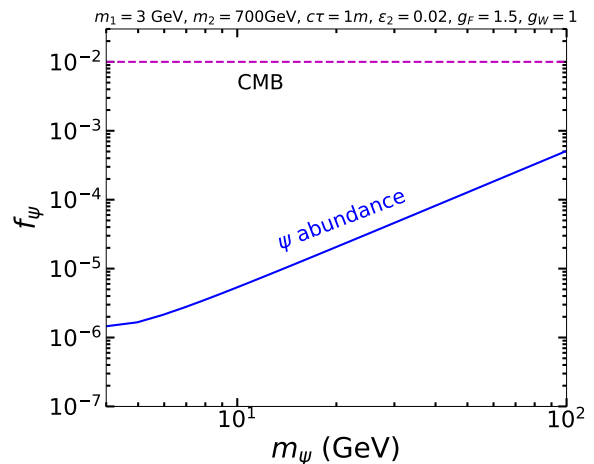


Figure 2. The fraction of ψ to the total DM in the Universe as a function of the ψ mass. Here, we take the canonical DM cross section is $\langle\sigma v\rangle_{\text{DM}} = 1$ pb. The magenta dashed line represents the current limit from Refs. [33–36].

[37]

$$\langle\sigma v\rangle_{\psi\bar{\psi}\rightarrow A'A'} \simeq \frac{(v_2^\psi)^4}{16\pi m_\psi^2} \frac{(1-r^2)^{3/2}}{(1-r^2/2)^2}, \quad (10)$$

where v_2^ψ is the coupling between the dark photon and ψ , as given in Eq. (5), and $r = m_{A'}/m_\psi$. We compute the ratio between the ψ relic abundance and the total DM relic abundance via $f_\psi = 2\langle\sigma v\rangle_{\text{DM}}/\langle\sigma v\rangle_{\psi\bar{\psi}\rightarrow A'A'}$, where $\langle\sigma v\rangle_{\text{DM}} = 1$ pb is the canonical DM cross section, and the factor of 2 accounts for the Dirac nature of the ψ particle. Because $v_2^\psi \simeq g_F$, the annihilation cross section given in Eq. (10) is much larger than the canonical annihilation cross section needed for the cold DM relic density in the Universe [38], for the case $m_{A'} \sim \mathcal{O}(1)$ GeV and $m_\psi \sim \mathcal{O}(10)$ GeV. Thus, the contribution of the ψ particle to the DM in the Universe is less 0.1% when $m_\psi < 100$ GeV, as shown in Fig. (2). This is consistent with the cosmological limits on millicharged DM, which constrain the fraction of the millicharged DM to be $\lesssim 1\%$ of the total DM in the Universe [33–36]. The ψ DM is efficiently stopped by the rock above underground labs of DM direct detection experiments, unless the millicharge is extremely small. Adapting the estimation in Refs. [39, 40] for 1 km of rock, we found that the DM direct detection is only sensitive to the mixing parameter of $\epsilon_2 < 10^{-6}$ in our model. Thus the current underground DM direct detection experiments do not constrain the model.

Monojet constraints: Searches for invisible particles which are produced in association with an initial state radiation (ISR) jet have been carried out at ATLAS [32] and CMS [41]. Here we recast the ATLAS result [32] to set constraints on our model. We use MadGraph5 aMC@NLO (MG5) [42] to generate events for the process

$pp \rightarrow \psi\bar{\psi}j$ which are then passed to Pythia 8 for showering and hadronization [22, 43, 44]. The Madanalysis 5 package [45, 46] is further used to analyze the ATLAS results [32]. We use the same detector cuts as in Ref. [32]; the optimal selection region for our model is found to be in the window: $E_T^{\text{miss}} \in (300, 350)$ GeV (the EM2 region in Ref. [32]). The 95% CL exclusion limit on ϵ_2 from the monojet channel in ATLAS [32] is shown in Fig. (1). When $m_\psi < m_Z/2$, the Z boson diagram, i.e., the $pp \rightarrow Zj \rightarrow \psi\bar{\psi}j$ process gives the dominant contribution to the monojet signal; when $m_\psi > m_Z/2$, the Z' boson diagram, i.e., the $pp \rightarrow Z'j \rightarrow \psi\bar{\psi}j$ becomes more important than the Z process. Because of the large Z' mass, the Z' boson diagram is suppressed as compared to the Z diagram. Thus the monojet channel only provides a comparable constraint to other constraints for $m_\psi < m_Z/2$.

As shown in Fig. (1), the electroweak constraint on the Z mass shift provides the best constraint to the parameter space of interest in our model, except for the $m_\psi \lesssim 0.6$ GeV region where collider constraints on millicharged particles become strong.

TIMING DETECTOR

Recently, some precision timing detectors are proposed to be installed at CMS [47], ATLAS [48, 49] and LHCb [50]. These timing detectors, which aim to reduce the pile-up rate at the high luminosity LHC (HL-LHC), can also be used in long-lived particle searches [51–54]. In this analysis, we focus on one of the timing detectors, the minimum ionizing particle (MIP) timing detector to be installed to the CMS detector (hereafter MTD CMS) [47], which has a ~ 30 pico-second timing resolution. At the MTD CMS, the timing detection layer, which is proposed to be installed between the inner tracker and the electromagnetic calorimeter, is about 1.17 m away from the beam axis and 6.08 m long in the beam axis direction. A time delay at the LHC due to long-lived particles can be measured by the new precision timing detectors, which can enhance the collider sensitivity to such models [51].

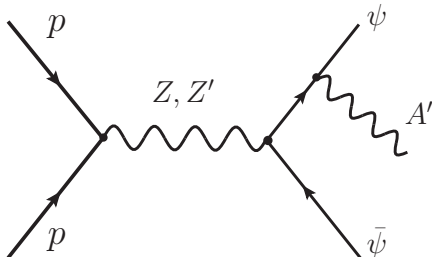


Figure 3. Feynman diagram for the dark photon production at the LHC.

At the LHC, the hidden sector particle ψ can be pair-produced via $pp \rightarrow Z/Z' \rightarrow \psi\bar{\psi}$, which subsequently radiates dark photons $\psi \rightarrow \psi A'$; the corresponding Feynman diagram is shown in Fig. (3). Due to the feeble interaction strength to SM fermions, the A' boson travels a macroscopic distance away from its production point and then decays into a pair of SM particles which are detected by the timing layers. Here we use the di-lepton final states measured by the timing layers to detect the LLDP in our model. The time delay between the leptons from the LLDP and SM particles produced at the primary vertex is given by

$$\Delta t = L_{A'}/v_{A'} + L_\ell - L_{\text{SM}}, \quad (11)$$

where the L 's are the distances traveled by various particles and $v = c$ for the SM particles [51]. The time delay is significant if the LLDP moves non-relativistically.

We select the leading leptons with transverse momentum $p_T^\ell > 3$ GeV to suppress faked signals from hadrons produced with low p_T [55] and to ensure that the lepton is moving relativistically and its trajectory is not significantly bent [51]. The point where the dark photon decays is required to have a radial distance away from the beam axis of $0.2 \text{ m} < L_{A'}^T < 1.17 \text{ m}$ and a longitudinal distance along the beam axis of $|z_{A'}| < 3.04 \text{ m}$. Following Ref. [51], an ISR jet with $p_T^j > 30$ GeV and $|\eta_j| < 2.5$ is required to time stamp the hard collision. The time delay is required to be $\Delta t > 1.2$ ns in order to suppress the background.

The dominant SM backgrounds come from the multi trackless jets in the same-vertex (SV) hard collisions and in the pile-up (PU) events [51], as well as photons in SV hard collisions [52]. The SV background arises because of the finite timing resolution; the PU background is due to the fact that within one bunch crossing, two hard collisions occurring at two different times can lead to a time delay signal.

We compute the dijet events at the LHC with $\sqrt{s} = 13$ TeV by using MG5 [42] and also Pythia 8 [43]. We select events in which the leading jet has $p_T > 30$ GeV and $|\eta(j)| < 2.5$ to time stamp the primary collision, and the subleading jets have $p_T^j > 3$ GeV and $|\eta(j)| < 2.5$. The inclusive jet cross section is $\sigma_j \approx 1 \times 10^8$ pb, under these detector cuts.

The inclusive photon production cross section at NLO is $\sigma_\gamma \approx 2 \times 10^8$ pb at the LHC with $\sqrt{s} = 13$ TeV, by using JETPHOX [56] with the CT10 PDF. The detector cuts are $p_T^\gamma > 3$ GeV and $|\eta^\gamma| < 2.5$ for photon and $p_T^j > 30$ GeV and $|\eta^j| < 2.5$ for the leading jet.

At the 13 TeV LHC, the SV background events can be estimated as [51, 52]

$$N_{\text{SV}} = \sigma_\gamma \mathcal{L} + \sigma_j \mathcal{L} f_\gamma \sim 6 \times 10^{14}, \quad (12)$$

where $\mathcal{L} = 3 \text{ ab}^{-1}$ is the integrated luminosity, and $f_\gamma \approx 10^{-4}$ is the rate of a jet to fake a photon or a lepton [52].

The PU background events can be estimated as [51, 52]

$$N_{\text{PU}} = \sigma_j \mathcal{L} (n_{\text{PU}} \frac{\sigma'_j}{\sigma_{\text{inc}}}) f_\gamma f_j \sim 3.75 \times 10^9, \quad (13)$$

where $f_j \sim 10^{-3}$ [52] is the rate for the jet to be trackless, $\sigma'_j \approx 1 \times 10^{11}$ pb is the dijet cross section with the requirement on all jets of $p_T^j > 3$ GeV and $|\eta(j)| < 2.5$, $\sigma_{\text{inc}} = 80$ mb [57] is the inelastic cross section of pp collisions at 13 TeV and $n_{\text{PU}} \approx 100$ [58] is the average pile-up number at the HL-LHC.

The time delay distribution of the SM background can be described by a Gaussian distribution [51]

$$\frac{d\mathcal{P}(\Delta t)}{d\Delta t} = \frac{1}{\sqrt{2\pi}\delta_t} e^{-\frac{\Delta t^2}{2\delta_t^2}}, \quad (14)$$

where δ_t is the time spread. For the PU background, the time spread, $\delta_t = 190$ ps, is determined by the beam property; for the SV background, $\delta_t = 30$ ps, is determined by the time resolution [47]. We find that under the detector cut $\Delta t > 1$ ns, the SV background is negligible and the PU background is about 260 with $\mathcal{L} = 3 \text{ ab}^{-1}$; the PU background also becomes negligible, $N_{\text{PU}} \lesssim 0.5$, if the time delay $\Delta t > 1.2$ ns is required. Thus, we take $\Delta t > 1.2$ ns as the detector cut in our analysis.

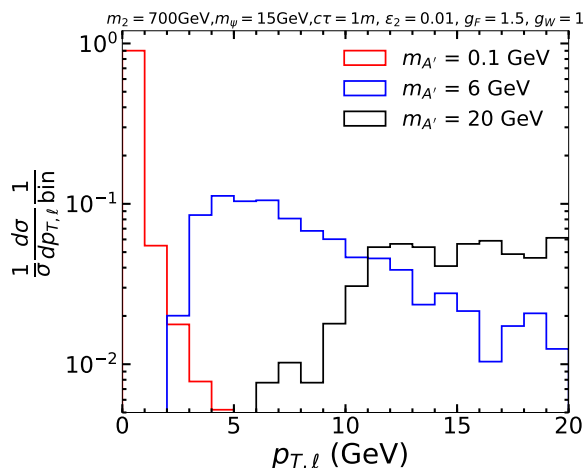


Figure 4. The p_T distribution of the leading lepton. We choose $m_2 = 700$ GeV, $m_\psi = 15$ GeV, $c\tau = 1$ m, $\epsilon_2 = 0.01$, $g_F = 1.5$ and $g_W = 1.0$. The red, blue and black lines indicate the dark photon mass of 0.1 GeV, 6 GeV and 20 GeV respectively.

We perform a full MC simulation and study the efficiency of the detector cuts in the parameter space of interest. We first implement the model into the FeynRules package [60] and pass the UFO model file into MG5 [42] to generate 8×10^4 events of the ψ pair production associated with the time stamping ISR jet i.e. $pp \rightarrow \psi\psi j$. The dark showering is simulated in Pythia 8 [22, 43, 44].

Fig. (4) shows the transverse momentum distribution of the leading lepton, for three different dark photon

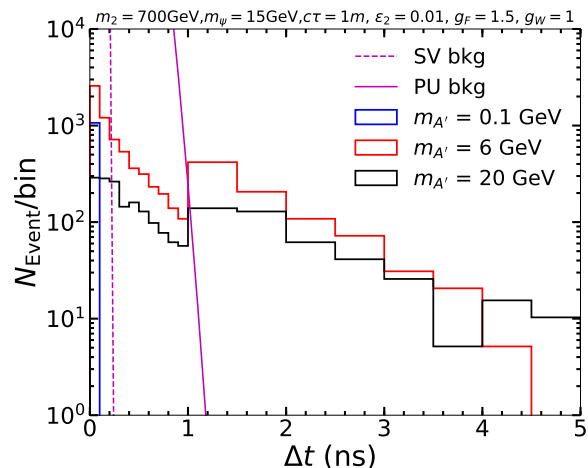


Figure 5. The distribution of the time delay Δt , with the integrated luminosity $\mathcal{L} = 3 \text{ ab}^{-1}$. $p_T > 3$ GeV is required for the leading lepton. The bin width is 0.5 (0.1) ns for $\Delta t > 1$ ns ($\Delta t < 1$ ns). We choose $m_2 = 700$ GeV, $m_\psi = 15$ GeV, $c\tau = 1$ m, $\epsilon_2 = 0.01$, $g_F = 1.5$ and $g_W = 1.0$. The solid blue, red and black lines indicate the dark photon mass of 0.1 GeV, 6 GeV and 20 GeV. The solid and dashed magenta curves represent the PU and SV backgrounds respectively.

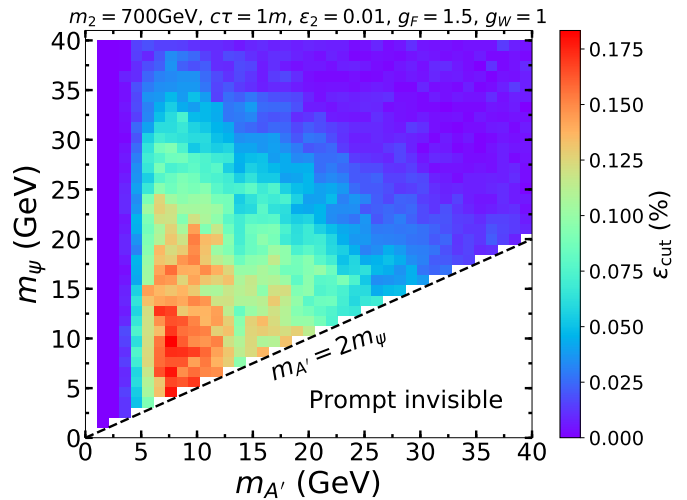


Figure 6. The cut efficiency ϵ_{cut} as a function of $m_{A'}$ and m_ψ . We set $m_2 = 700$ GeV, $c\tau = 1$ m, $\epsilon_2 = 0.01$, $g_F = 1.5$ and $g_W = 1.0$.

masses. We choose $m_2 = 700$ GeV, $m_\psi = 15$ GeV, $c\tau = 1$ m, $\epsilon_2 = 0.01$, $g_F = 1.5$ and $g_W = 1.0$, as the benchmark point. The final state leptons from dark photon decays are generally not very energetic in the models shown in Fig. (4). In particular, the lepton events are highly suppressed under the detector cut $p_T > 3$ GeV, for the 0.1 GeV dark photon case.

Fig. (5) shows the distribution of the time delay Δt . The model parameters in Fig. (5) are the same as in Fig. (4). The SM backgrounds are negligible when the

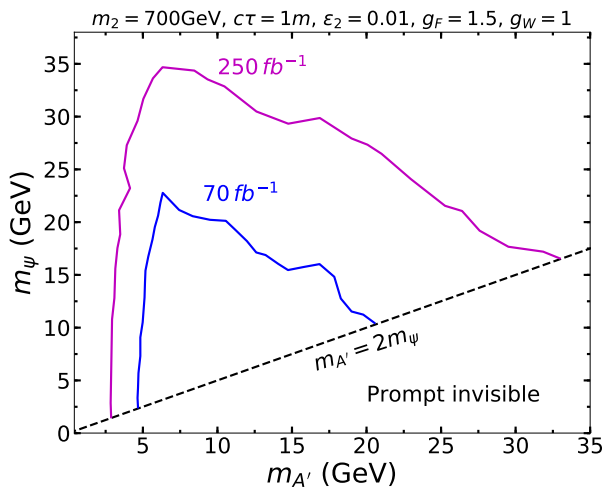


Figure 7. The contour of the expected signal events at the 13 TeV LHC, as a function of $m_{A'}$ and m_{ψ} . We choose $m_2 = 700$ GeV, $c\tau = 1$ m, $\epsilon_2 = 0.01$, $g_F = 1.5$ and $g_W = 1.0$. The blue and magenta contours indicate the needed integrated luminosity of 70 fb^{-1} and 250 fb^{-1} respectively, to generate 10 events.

time delay $\Delta t > 1.2$ ns. When the dark photon becomes heavier, more events with a larger time delay appear, as shown in Fig. (5), since in this case, the dark photon has a higher probability to move non-relativistically. The increase of the events with the larger time delay, however, is offset by the smaller dark photon radiation rate of the heavier dark photon.

Fig. (6) shows the cut efficiency as a function of $m_{A'}$ and m_{ψ} , where 1370 grid points are simulated. We set $m_2 = 700$ GeV, $c\tau = 1$ m, $\epsilon_2 = 0.01$, $g_F = 1.5$ and $g_W = 1.0$. As shown in Fig. (4), the detector cut: $p_T > 3$ GeV for the leading lepton, significantly reduces the efficiency for light dark photon mass. The low efficiency in the heavy mass region in Fig. (6) is primarily due to the low radiation rate [61]. It turns out that the region with significant cut efficiency has $5 \text{ GeV} < m_{A'}, m_{\psi} < 35 \text{ GeV}$, with the highest efficiency $\sim 0.18\%$. We note that, for the $m_{A'} > 2m_{\psi}$ region, the dark photon is no longer a long-lived particle since it can decay into a pair of ψ .

Fig. (7) shows the regions that can be probed at the 13 TeV LHC, with the discovery criterion: $S = 10$, as a function of the dark photon mass and the ψ mass. The number of signal events is computed via $S = \epsilon_{\text{cut}} \mathcal{L} \sigma(pp \rightarrow \psi\bar{\psi}j)$, where \mathcal{L} is the integrated luminosity, $\sigma(pp \rightarrow \psi\bar{\psi}j)$ is the production cross section at the LHC, and ϵ_{cut} is the cut efficiency as shown in Fig. (6). The model parameters are the same as in Fig. (6). The blue and magenta contours indicate the needed integrated luminosity to generate 10 signal events. Therefore, with an integrated luminosity of 70 fb^{-1} at the HL-LHC, the LLDP can be discovered in the time delay channel in the mass

region: $5 \text{ GeV} < m_{A'}, m_{\psi} < 21 \text{ GeV}$, with the rest of the model parameters fixed as in Fig. (6). A larger mass region: $3 \text{ GeV} < m_{A'}, m_{\psi} < 30 \text{ GeV}$, can be discovered if 250 fb^{-1} data are accumulated at the HL-LHC.

Fig. (8) shows the integrated luminosity needed to probe the parameter space spanned by ϵ_2 and $m_{Z'}$. We choose $m_1 = 6$ GeV, $m_{\psi} = 15$ GeV, $c\tau = 1$ m, $g_F = 1.5$ and $g_W = 1$ as a benchmark. With an integrated luminosity of $\sim 4.0 \text{ fb}^{-1}$, one can probe the ϵ_2 value that saturates the electroweak constraint on the Z mass shift. To discover a long-lived dark photon model in which $\epsilon_2 \simeq 10^{-3}$, however, one needs about 3000 fb^{-1} data at the HL-LHC. When $\epsilon_2 \simeq \mathcal{O}(10^{-7})$, the LLDP signal approaches the value in the conventional LLDP scenario, so that it is no longer enhanced by the production channel mediated by the ϵ_2 parameter.

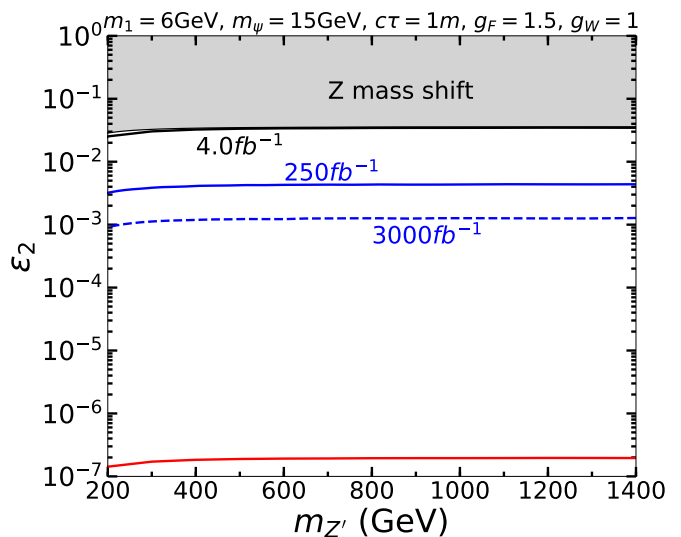


Figure 8. The integrated luminosity needed at the HL-LHC to probe the parameter region spanned by $m_{Z'}$ and ϵ_2 . We choose $m_1 = 6$ GeV, $m_{\psi} = 15$ GeV, $c\tau = 1$ m, $g_F = 1.5$ and $g_W = 1$. The integrated luminosity needed are $\sim 4.0 \text{ fb}^{-1}$ (black solid), 250 fb^{-1} (blue solid), and 3000 fb^{-1} (blue dashed). The gray shaded region is excluded by the Z mass shift constraint, as given in Eq. (9). Below the red line, the dark photon production cross section via ϵ_1 dominates.

LHCb

Due to the excellent mass resolution (7-20 MeV) and vertex resolution ($\sim 10 \mu\text{m}$ on the transverse plane) as well as the ability for particle identification ($\sim 90\%$ for muons) [63, 64], the LHCb detector is able to discover new elusive particles beyond the SM. An upcoming upgrade with an increased luminosity and a more advanced trigger system with only software triggers will further improve the capability of the LHCb detector to probe new physics phenomena, such as LLDPs [64]. Recently,

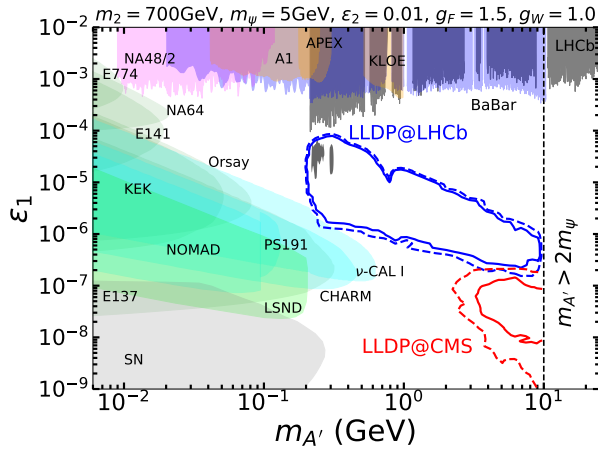


Figure 9. LHC current and future sensitivity contours to the LLDP parameter space spanned by ϵ_1 and the dark photon mass. We take $m_\psi = 5$ GeV and $\epsilon_2 = 0.01$. The blue solid and dashed contours indicate the regions probed by the LHCb with 5.5 fb^{-1} and 15 fb^{-1} data respectively. The regions probed by the future MTD CMS with 250 fb^{-1} and 3000 fb^{-1} data are shown as red solid and dashed contours respectively. The gray islands at $\epsilon_1 \sim (10^{-4} - 10^{-5})$ are the LHCb exclusion regions for the conventional dark photon scenario [62]. Various experimental constraints on the conventional dark photon scenario are shown as color shaded regions.

a search for LLDPs in the kinetic mixing model has been carried out at the LHCb via displaced muon pairs [62, 65, 66]. In our model, because LLDPs has a larger production cross section at the LHC than the conventional LLDP models, the LHCb search [62] can probe a much larger parameter space.

To analyze the LHCb constraints, we choose a benchmark point in which $m_\psi = 5$ GeV and $\epsilon_2 = 0.01$, while the rest of the parameters take the default values. In this benchmark point, the ψ production cross section, $\sigma(pp \rightarrow \psi\bar{\psi}) \sim 4.3$ pb which is dominated by the Z -boson exchange channel. We use MG5 [42] to generate the LHC events for each model point on the ϵ_1 - $m_{A'}$ plane, which are then passed to Pythia 8 [22, 43, 44] for showering (including showering in hidden sector) and hadronization.

We follow the LLDP search criteria in Ref. [62, 66] to analyze the signal. In particular, we require the transverse distance of the dark photon decay vertex of $6 \text{ mm} < l_T(A') < 22 \text{ mm}$ and the pseudo-rapidity of dark photons and muons of $2 < \eta(A', \mu^\pm) < 4.5$. These requirements ensure that the displaced vertex is sufficiently separated from the beam line and registered in the Vertex Locator (VELO) where the dimuon can be reconstructed with good efficiency. Furthermore, in order to suppress the background from fake muons, we also require the momentum and transverse momentum of muons are greater than 10 GeV and 0.5 GeV respectively.

The dominant background includes the photon-conversion in the VELO, muons produced from b-hadron

decay chains, and pions from K_s^0 decays which are misidentified as muons. Ref. [65] estimated the background events as $B = 25$ for $\mathcal{L} = 15 \text{ fb}^{-1}$, which is adopted in our analysis and also rescaled for the $\mathcal{L} = 5.5 \text{ fb}^{-1}$ case. We compute the exclusion region by demanding that $S/\sqrt{B} > 2.71$ where S is the signal event number.

Fig. (9) shows the LHCb exclusion region in the parameter space spanned by ϵ_1 and the dark photon mass $m_{A'}$. With the current luminosity 5.5 fb^{-1} , LHCb can probe the parameter space of our model: $200 \text{ MeV} < m_{A'} < 9 \text{ GeV}$ and $2 \times 10^{-7} < \epsilon_1 < 6 \times 10^{-5}$. The exclusion region in the conventional dark photon scenario is, however, much smaller, which is shown as two small gray islands at $\epsilon_1 \sim (10^{-4} - 10^{-5})$. Thus, in our model, a significantly larger region of parameter space than the conventional dark photon model can be probed by the current LLDP search at the LHCb. A projected limit from the Run 3 data is also computed; LHCb can probe the parameter space: $200 \text{ MeV} < m_{A'} < 10 \text{ GeV}$ and $10^{-7} < \epsilon_1 < 10^{-4}$, if 15 fb^{-1} integrated luminosity can be accumulated in the LHC Run 3 data. We note in passing that the shape of the exclusion contours is primarily due to the detector cut on the dark photon decay length: a smaller ϵ_1 value is needed in the larger dark photon mass region so that the dark photon has the desired decay width to disintegrate in the VELO region. Also the dip at $m_{A'} \simeq 0.8$ GeV is due to the ω resonance which suppresses the $\text{BR}(A' \rightarrow \mu^+\mu^-)$. Fig. (9) also shows the exclusion limits on the conventional dark photon from various experiments; the limits are taken from the Darkcast package [67].

Fig. (9) also shows the sensitivities from the future MTD CMS detector via the time delay measurement. As mentioned before, the time delay signal from the final state leptons becomes more significant if the LLDPs have long lifetime and move non-relativistically. Therefore, the timing detector probes the heavy dark photon mass region with a smaller mixing parameter ϵ_1 which are currently almost inaccessible at the LHCb. In particular, with the luminosity of 250 fb^{-1} at the HL-LHC, the MTD CMS detector can probe the parameter space: $m_{A'} > 3.3 \text{ GeV}$ and $10^{-8} < \epsilon_1 < 10^{-7}$. An even larger parameter space in our model: $m_{A'} > 2.0 \text{ GeV}$ and $10^{-9} < \epsilon_1 < 2 \times 10^{-7}$, can be reached with 3000 fb^{-1} data accumulated at the HL-LHC. Interestingly, this MTD CMS sensitivity region partly overlaps with the LHCb sensitivity region with 15 fb^{-1} data. Thus, if the LLDP is discovered in this overlapped region, the timing detector can be used to verify the LHCb results. We note that, in the region of $m_{A'} > 2m_\psi$, the dark photon will dominantly decay into ψ so that it can no longer be searched for in the visible channel by the LHCb detector and the future precision timing detectors.

SUMMARY

We construct a long-lived dark photon model which has an enhanced dark photon collider signal. We extend the standard model by a hidden sector which has two gauge bosons and one Dirac fermion ψ ; the two gauge bosons interact with the SM sector via different Stueckelberg mass terms. The GeV-scale dark photon A' interacts with the SM fermions via a very small Stueckelberg mass term (parametrized by the dimensionless quantity ϵ_1) such that it has a macroscopic decay length which can lead to a displaced vertex or a time delay signal at the LHC. The TeV-scale Z' boson interacts with the SM via a relatively larger mass term (parametrized by the dimensionless quantity ϵ_2). Because the dark photon A' is mainly produced at the LHC via the ψ dark radiation processes in which the effective coupling strength is of the size of ϵ_2 the LHC signal of A' is thus enhanced significantly.

Various experimental constraints on the model are analyzed, including the electroweak constraint on the Z boson mass shift, the constraint from the Z invisible decay, LHC constraints, collider constraints on millicharge, and cosmological constraints on millicharge. The electroweak constraint on the Z mass turns out to be the most stringent one, which leads to an upper bound $\epsilon_2 \lesssim 0.036$, in the parameter space of interest.

Two types of LHC signals from the LLDP in our model are investigated: the time delay signal measured by the precision timing detectors at the HL-LHC, and the current LHCb searches on LLDPs. If the LLDP is produced non-relativistically at the LHC, it has a significant time delay Δt , which can be measured by the precision timing detectors. Under the detector cut $\Delta t > 1.2$ ns, the SV and PU backgrounds are found to be negligible. The parameter space of $3 \text{ GeV} < m_{A'}, m_\psi < 30 \text{ GeV}$ in our model is found to be probed by the timing detector with 250 fb^{-1} data at the HL-LHC.

Due to the different search strategy, the current LHCb analysis is more sensitive to the lighter dark photon mass than the time delay searches. We found that the parameter space probed by the current LHCb analysis is much larger in our model than the conventional dark photon model investigated in the LHCb experimental analysis. A comparison between the LHCb search and the time delay search is also made; they typically probe different regions of the parameter space but can overlap in some small regions.

We note that a similar model as ours can be constructed by introducing two kinetic mixing parameters, of magnitude $\mathcal{O}(10^{-2})$ and $\mathcal{O}(10^{-7})$, which are responsible for dark photon production and decay processes, respectively.

ACKNOWLEDGEMENT

We thank Jinhan Liang and Lei Zhang for helpful discussions and correspondence. The work is supported in part by the National Natural Science Foundation of China under Grant Nos. 11775109 and U1738134.

* zuoweiliu@nju.edu.cn

- [1] J. Alimena *et al.*, arXiv:1903.04497 [hep-ex].
- [2] G. Aad *et al.* [ATLAS Collaboration], Phys. Rev. D **92**, no. 7, 072004 (2015) [arXiv:1504.05162 [hep-ex]].
- [3] M. Aaboud *et al.* [ATLAS Collaboration], Phys. Rev. D **99**, no. 1, 012001 (2019) [arXiv:1808.03057 [hep-ex]].
- [4] V. Khachatryan *et al.* [CMS Collaboration], Phys. Rev. D **91**, no. 5, 052012 (2015) [arXiv:1411.6977 [hep-ex]].
- [5] V. Khachatryan *et al.* [CMS Collaboration], Phys. Rev. Lett. **114**, no. 6, 061801 (2015) [arXiv:1409.4789 [hep-ex]].
- [6] G. Aad *et al.* [ATLAS Collaboration], arXiv:1907.10037 [hep-ex].
- [7] G. Aad *et al.* [ATLAS Collaboration], Eur. Phys. J. C **72**, 1965 (2012) [arXiv:1201.5595 [hep-ex]].
- [8] S. Chatrchyan *et al.* [CMS Collaboration], Phys. Lett. B **713**, 408 (2012) [arXiv:1205.0272 [hep-ex]].
- [9] G. Aad *et al.* [ATLAS Collaboration], Phys. Rev. D **88**, no. 11, 112003 (2013) [arXiv:1310.6584 [hep-ex]].
- [10] V. Khachatryan *et al.* [CMS Collaboration], Eur. Phys. J. C **75**, no. 4, 151 (2015) [arXiv:1501.05603 [hep-ex]].
- [11] M. Aaboud *et al.* [ATLAS Collaboration], Phys. Rev. D **93**, no. 11, 112015 (2016) [arXiv:1604.04520 [hep-ex]].
- [12] V. Khachatryan *et al.* [CMS Collaboration], Phys. Rev. D **94**, no. 11, 112004 (2016) [arXiv:1609.08382 [hep-ex]].
- [13] M. Aaboud *et al.* [ATLAS Collaboration], Phys. Rev. D **97**, no. 5, 052012 (2018) [arXiv:1710.04901 [hep-ex]].
- [14] M. Aaboud *et al.* [ATLAS Collaboration], Eur. Phys. J. C **79**, no. 6, 481 (2019) [arXiv:1902.03094 [hep-ex]].
- [15] CMS Collaboration [CMS Collaboration], CMS-PAS-EXO-19-001.
- [16] G. Aad *et al.* [ATLAS Collaboration], JHEP **1411**, 088 (2014) [arXiv:1409.0746 [hep-ex]].
- [17] G. Aad *et al.* [ATLAS Collaboration], arXiv:1909.01246 [hep-ex].
- [18] M. Buschmann, J. Kopp, J. Liu and P. A. N. Machado, JHEP **1507**, 045 (2015) [arXiv:1505.07459 [hep-ph]].
- [19] C. A. Argelles, X. G. He, G. Ovanessian, T. Peng and M. J. Ramsey-Musolf, Phys. Lett. B **770**, 101 (2017) [arXiv:1604.00044 [hep-ph]].
- [20] J. H. Kim, S. D. Lane, H. S. Lee, I. M. Lewis and M. Sullivan, arXiv:1904.05893 [hep-ph].
- [21] A. Krovi, I. Low and Y. Zhang, arXiv:1909.07987 [hep-ph].
- [22] L. Carloni and T. Sjostrand, JHEP **1009**, 105 (2010) [arXiv:1006.2911 [hep-ph]].
- [23] B. Kors and P. Nath, JHEP **0507**, 069 (2005) [hep-ph/0503208].
- [24] D. Feldman, Z. Liu and P. Nath, Phys. Rev. Lett. **97**, 021801 (2006) [hep-ph/0603039].
- [25] D. Feldman, Z. Liu and P. Nath, JHEP **0611**, 007 (2006) [hep-ph/0606294].

- [26] D. Feldman, Z. Liu and P. Nath, Phys. Rev. D **75**, 115001 (2007) [hep-ph/0702123 [HEP-PH]].
- [27] D. Feldman, Z. Liu, P. Nath and B. D. Nelson, Phys. Rev. D **80**, 075001 (2009) [arXiv:0907.5392 [hep-ph]].
- [28] S. Schael *et al.* [ALEPH and DELPHI and L3 and OPAL and SLD Collaborations and LEP Electroweak Working Group and SLD Electroweak Group and SLD Heavy Flavour Group], Phys. Rept. **427**, 257 (2006) [hep-ex/0509008].
- [29] M. Tanabashi *et al.* [Particle Data Group], Phys. Rev. D **98**, no. 3, 030001 (2018).
- [30] The ATLAS collaboration [ATLAS Collaboration], ATLAS-CONF-2019-001.
- [31] S. Davidson, S. Hannestad and G. Raffelt, JHEP **0005**, 003 (2000) [hep-ph/0001179].
- [32] M. Aaboud *et al.* [ATLAS Collaboration], JHEP **1801**, 126 (2018) [arXiv:1711.03301 [hep-ex]].
- [33] J. B. Muoz and A. Loeb, Nature **557**, no. 7707, 684 (2018) [arXiv:1802.10094 [astro-ph.CO]].
- [34] K. K. Boddy, V. Gluscevic, V. Poulin, E. D. Kovetz, M. Kamionkowski and R. Barkana, Phys. Rev. D **98**, no. 12, 123506 (2018) [arXiv:1808.00001 [astro-ph.CO]].
- [35] R. de Putter, O. Dor, J. Gleyzes, D. Green and J. Meyers, Phys. Rev. Lett. **122**, no. 4, 041301 (2019) [arXiv:1805.11616 [astro-ph.CO]].
- [36] E. D. Kovetz, V. Poulin, V. Gluscevic, K. K. Boddy, R. Barkana and M. Kamionkowski, Phys. Rev. D **98**, no. 10, 103529 (2018) [arXiv:1807.11482 [astro-ph.CO]].
- [37] J. M. Cline, G. Dupuis, Z. Liu and W. Xue, JHEP **1408**, 131 (2014) [arXiv:1405.7691 [hep-ph]].
- [38] P. A. R. Ade *et al.* [Planck Collaboration], Astron. Astrophys. **594**, A13 (2016) [arXiv:1502.01589 [astro-ph.CO]].
- [39] R. Foot, Phys. Rev. D **69**, 036001 (2004) [hep-ph/0308254].
- [40] J. M. Cline, Z. Liu and W. Xue, Phys. Rev. D **85**, 101302 (2012) [arXiv:1201.4858 [hep-ph]].
- [41] A. M. Sirunyan *et al.* [CMS Collaboration], Phys. Rev. D **97**, no. 9, 092005 (2018) [arXiv:1712.02345 [hep-ex]].
- [42] J. Alwall *et al.*, JHEP **1407**, 079 (2014) [arXiv:1405.0301 [hep-ph]].
- [43] T. Sjstrand *et al.*, Comput. Phys. Commun. **191**, 159 (2015) [arXiv:1410.3012 [hep-ph]].
- [44] L. Carloni, J. Rathsman and T. Sjostrand, JHEP **1104**, 091 (2011) [arXiv:1102.3795 [hep-ph]].
- [45] B. Dumont *et al.*, Eur. Phys. J. C **75**, no. 2, 56 (2015) [arXiv:1407.3278 [hep-ph]].
- [46] D. Sengupta, doi:10.7484/INSPIREHEP.DATA.HUH5.239F
- [47] C. Collaboration, Tech. Rep. CERN-LHCC-2017-027. LHCC-P-009, CERN, Geneva, Dec, 2017. <https://cds.cern.ch/record/2296612>.
- [48] C. Allaire *et al.*, JINST **13**, no. 06, P06017 (2018) [arXiv:1804.00622 [physics.ins-det]].
- [49] C. Allaire [ATLAS LAr-HGTD Group], Nucl. Instrum. Meth. A **924**, 355 (2019).
- [50] R. e. a. Aaij (LHCb Collaboration), Technical Report No. CERN-LHCC-2017-003, CERN, Geneva, 2017, <http://cds.cern.ch/record/2244311>.
- [51] J. Liu, Z. Liu and L. T. Wang, Phys. Rev. Lett. **122**, no. 13, 131801 (2019) [arXiv:1805.05957 [hep-ph]].
- [52] J. D. Mason, JHEP **1907**, 089 (2019) [arXiv:1905.07772 [hep-ph]].
- [53] Z. Flowers, D. W. Kang, Q. Meier, S. C. Park and C. Rogan, arXiv:1903.05825 [hep-ph].
- [54] O. Cerri, S. Xie, C. Pena and M. Spiropulu, JHEP **1904**, 037 (2019) [arXiv:1807.05453 [hep-ex]].
- [55] A. M. Sirunyan *et al.* [CMS Collaboration], Phys. Rev. D **96**, no. 11, 112003 (2017) [arXiv:1706.10194 [hep-ex]].
- [56] S. Catani, M. Fontannaz, J. P. Guillet and E. Pilon, JHEP **0205**, 028 (2002) [hep-ph/0204023].
- [57] M. Aaboud *et al.* [ATLAS Collaboration], Phys. Rev. Lett. **117**, no. 18, 182002 (2016) [arXiv:1606.02625 [hep-ex]].
- [58] A. Sopczak *et al.*, IEEE Trans. Nucl. Sci. **64**, no. 3, 915 (2017) [arXiv:1702.00711 [physics.ins-det]].
- [59] V. Khachatryan *et al.* [CMS Collaboration], JHEP **1703**, 156 (2017) [arXiv:1609.05331 [hep-ex]].
- [60] A. Alloul, N. D. Christensen, C. Degrande, C. Duhr and B. Fuks, Comput. Phys. Commun. **185**, 2250 (2014) [arXiv:1310.1921 [hep-ph]].
- [61] J. Chen, P. Ko, H. N. Li, J. Li and H. Yokoya, JHEP **1901**, 141 (2019) [arXiv:1807.00530 [hep-ph]].
- [62] R. Aaij *et al.* [LHCb Collaboration], arXiv:1910.06926 [hep-ex].
- [63] R. Aaij *et al.* [LHCb Collaboration], JHEP **1603**, 159 (2016) Erratum: [JHEP **1609**, 013 (2016)] Erratum: [JHEP **1705**, 074 (2017)] [arXiv:1510.01707 [hep-ex]].
- [64] S. Benson, V. V. Gligorov, M. A. Vesterinen and M. Williams, J. Phys. Conf. Ser. **664**, no. 8, 082004 (2015).
- [65] P. Ilten, Y. Soreq, J. Thaler, M. Williams and W. Xue, Phys. Rev. Lett. **116**, no. 25, 251803 (2016) [arXiv:1603.08926 [hep-ph]].
- [66] R. Aaij *et al.* [LHCb Collaboration], Phys. Rev. Lett. **120**, no. 6, 061801 (2018) [arXiv:1710.02867 [hep-ex]].
- [67] <https://gitlab.com/philtlen/darkcast>

Decay and Lifetime of Dark Photon A'

The dark photon leptonic decay width is given by

$$\Gamma(A' \rightarrow l^+l^-) = \frac{m_{A'}}{12\pi} \sqrt{1 - 4\frac{m_l^2}{m_{A'}^2}} \left[\left(1 - 4\frac{m_l^2}{m_{A'}^2}\right) |a_2^l|^2 + \left(1 + 2\frac{m_l^2}{m_{A'}^2}\right) |v_2^l|^2 \right], \quad (15)$$

where v_2^l and a_2^l are the vector and axial-vector couplings between the dark photon and the leptons which are given in Eqs. (4,5). The hadronic decay width can be computed by

$$\Gamma(A' \rightarrow \text{hadrons}) = \Gamma(A' \rightarrow \mu^+\mu^-) R(m_{A'}^2), \quad (16)$$

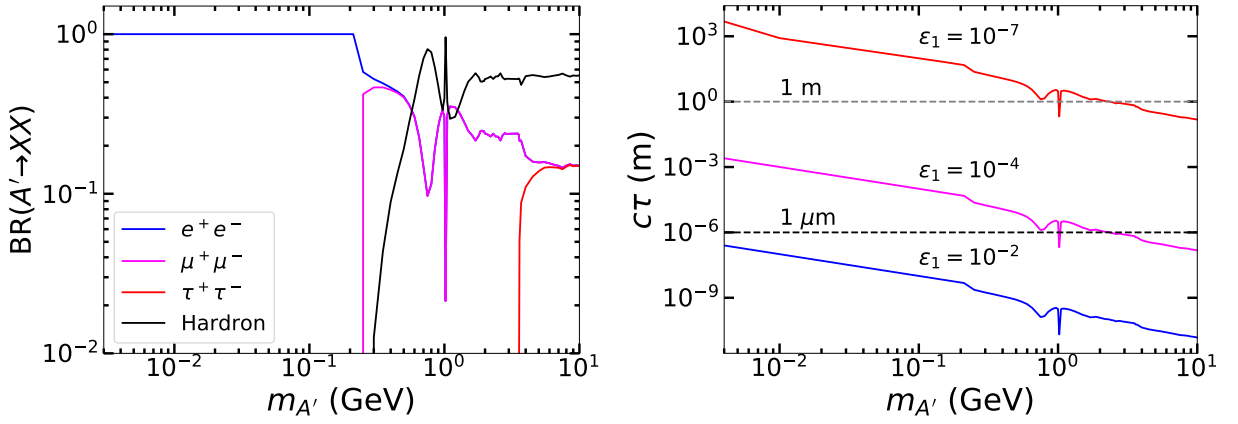


Figure 10. Left panel: Branching ratio of the dark photon. Right panel: Proper lifetime of the dark photon with various values of ϵ_1 . The dashed black line on the right panel figure indicates the criterion for the LHC prompt decay: $c\tau \leq 1 \mu\text{m}$.

where $R(m_{A'}^2) \equiv \sigma(e^+e^- \rightarrow \text{hadrons})/\sigma(e^+e^- \rightarrow \mu^+\mu^-)$ takes into account the effects of the dark photon mixing with the QCD vector mesons and is taken from Ref. [29]. The $\Gamma(A' \rightarrow \psi\bar{\psi})$ can be computed by replacing the couplings and mass for leptons in Eq. (15) with the ones for ψ . We note that below a few hundred MeV, dark photon decays into the e^+e^- and $\mu^+\mu^-$ pairs. In our analysis, since we consider $m_{A'} < 2m_\psi$, the $\Gamma(A' \rightarrow \psi\bar{\psi})$ is kinematically forbidden.

Fig. (10) shows the SM branching ratios of the dark photon decay and its proper lifetime with different ϵ_1 values. We note that a particle is considered as a long-lived particle in particle colliders if its decay length is larger than the detector spatial resolution which can vary from $\mathcal{O}(10)\mu\text{m}$ to $\mathcal{O}(10)\text{mm}$ depending on the detectors.